ACS APPLIED MATERIALS & INTERFACES

www.acsami.org

Research Article

Interlocked Hemispherical–Conical Porous Dielectric Layers for High-Sensitivity and Wide-Range Capacitive Pressure Sensing

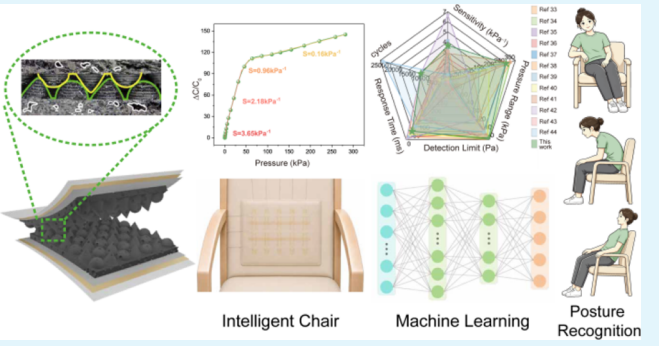
Shiqi Wu,‡ Yanyan Chen,‡ Jiawei Wu, Junseong Ahn, Yun-Woo Lee, Hongbo Wang, Bingjun Yu, Caijiang Lu, and Zhi-Jun Zhao*

Cite This: *ACS Appl. Mater. Interfaces* 2026, 18, 45605–45617

Read Online

ACCESS | Metrics & More | Article Recommendations | Supporting Information

ABSTRACT: Flexible capacitive pressure sensors demand high sensitivity across a broad detection range to simultaneously capture subtle physiological signals and macroscopic mechanical stimuli. Nevertheless, dielectric layers engineered to enhance low-pressure sensitivity typically suffer from structural densification and response saturation under high pressure, resulting in an inevitable trade-off between sensitivity and sensing range. Herein, we present a flexible capacitive pressure sensor featuring a rationally designed poly(dimethylsiloxane)/multiwalled carbon nanotube (PDMS/MWCNT) composite dielectric layer. This layer utilizes an interlocking double-layer architecture characterized by interlaced hemispherical and conical protrusions alongside internal pores. Under compression, this structure undergoes stepwise deformation via local contact enhancement, interlayer interlocking, and pore collapse, thereby enhancing the capacitive response across a broad pressure range. Consequently, it enables multiscale monitoring, ranging from subtle physiological signals to robust joint motions and gripping forces. Furthermore, a chair-integrated 3 × 5 sensor array achieved low-crosstalk spatial pressure mapping and recognized five typical sitting postures with 98.82% accuracy. This work offers a powerful structural strategy for broad-range intelligent pressure sensors, promising for diverse human–machine interaction applications.



KEYWORDS: *flexible capacitive pressure sensor, heterogeneous interlocked structure, high sensitivity, wearable sensing, sitting posture recognition, machine learning*

1. INTRODUCTION

Flexible pressure sensors have attracted widespread attention because of their potential applications in wearable health monitoring,[1,2] electronic skin,[3] and human–machine interaction.[4,5] In practical applications, monitoring human activities—ranging from subtle physiological pulses (pascal level) to robust joint kinematics and sitting posture distributions (hundred-kilopascal level)—involves multiscale mechanical stimuli. This demands sensors capable of delivering both ultrahigh resolution in the low-pressure regime and stable signal acquisition under high-pressure loading. Compared with resistive,[6,7] piezoelectric,[8,9] and triboelectric[10,11] pressure sensors, capacitive pressure sensors[12,13] offer advantages such as simple structure, low power consumption, fast dynamic response, and high signal stability.[14,15] Nevertheless, achieving an optimal balance between high sensitivity and a broad detection range remains a formidable challenge.[16,17] High sensitivity typically relies on low-modulus dielectrics and localized stress concentrations, which inadvertently cause rapid structural densification and signal saturation at low pressures. Conversely, a broad sensing range requires robust elastic support and sufficient compressible volume under heavy loads. Bridging this gap remains a critical challenge for multiscale pressure monitoring. Sensor optimization traditionally focuses on the structural engineering of the dielectric layer. Surface microstructures—such as micro-pyramids,[18] micropillars,[19] and cylindrical ladders—are frequently deployed to lower the initial compressive modulus and amplify low-pressure sensitivity.[20] For instance, Thouti et al.[21] developed a micro-pyramidal dielectric achieving 0.16 kPa^{-1} below 1 kPa, yet its operational range was restricted to 0–2.5 kPa. To mitigate this, Hua et al.[22] introduced a cylindrical ladder geometry, extending the measurable range to 300 kPa. While these topographies effectively enhance initial capacitive responses, their sensing mechanisms are

Received: May 27, 2026
Revised: July 13, 2026
Accepted: August 4, 2026
Published: August 11, 2026



Downloaded from pubs.acs.org/aamick/article-pdf/18/33/45605/6650371 1/am-2026-10724g.pdf by KOREA UNIV user on 23 September 2026

ACS Publications

© 2026 American Chemical Society

ultimately constrained by protrusion compression. Upon reaching higher pressures, the microstructures compact, leaving insufficient free space for further deformation and abruptly halting capacitance variation.

To defer structural densification, internal porous architectures have been integrated to supply auxiliary compressible voids.[23] Hwang et al.[24] demonstrated a hierarchically porous PDMS composite with a broad range of 0−400 kPa. Although internal pores drastically improve bulk compressibility, they lack the geometric precision required to govern local stress concentrations and maximize initial low-pressure sensitivity. Consequently, synergistic approaches combining surface microstructures with internal pores have emerged. For example, Kim et al.[25] engineered a cone-patterned porous dielectric, achieving 5 kPa^{-1} within 0−5 kPa. Despite these advances, existing hybrid dielectrics primarily rely on decoupled deformation modes. They lack a progressive, hierarchically organized architecture capable of continuously modulating local contact, interfacial interlocking, and internal void collapse across the entire pressure spectrum. Beyond geometry, material composition is pivotal. Poly(dimethylsiloxane) (PDMS) is the premier dielectric matrix owing to its inherent elasticity and biocompatibility.[26,27] Doping PDMS with multiwalled carbon nanotubes (MWCNTs) enhances the effective permittivity via interfacial polarization, thereby amplifying the baseline capacitance response.[28] However, heavily relying on conductive fillers is mechanically inadequate for broad-range sensing and introduces risks of filler agglomeration, high dielectric loss, and compromised compliance. Thus, compositional enhancements must be intrinsically linked with hierarchically compressible structural designs.

To overcome the inherent trade-off between sensitivity and detection range, we propose a flexible capacitive sensor based on a synergistic material−structural engineering strategy. Utilizing a PDMS/MWCNT nanocomposite, we engineered a double-layer interlocked dielectric featuring staggered hemispherical and conical protrusions, integrated with internal porous networks. The key advantage of this architecture lies in its continuous, multistage deformation pathway. Under low pressures, the conical protrusions induce acute localized stress, maximizing the initial sensitivity. Under moderate pressures, the hemispherical protrusions provide essential elastic support, while the interlocked interface drives a coupled expansion of the contact area and a reduction in electrode distance. Under high pressures, the internal pores undergo progressive collapse, which effectively delays macroscopic densification and prevents early response saturation. This hierarchical deformation mechanism guarantees a highly tunable capacitive response over an exceptionally broad pressure domain. Benefiting from this rational design, the optimized sensor delivers reliable performance across a 0−280 kPa range, achieving a low-pressure sensitivity of 3.65 kPa^{-1} and a low detection limit of 1.22 Pa. It seamlessly transitions from capturing faint physiological pulses to monitoring large-scale human kinematics. Furthermore, integrated sensor arrays, coupled with a backpropagation (BP) neural network, successfully realize low-crosstalk spatial pressure mapping and high-accuracy sitting posture recognition (98.82%). This work presents a highly effective structural paradigm for developing multiscale pressure sensors in smart wearables and human−machine interactions.

2. RESULTS AND DISCUSSION

2.1. Structural Design and Sensing Mechanism

Figure 1a illustrates the architecture of the heterogeneous interlocked hemispherical−conical staggered porous sensor (HI-HCPS). The device comprises a PDMS/MWCNT composite dielectric sandwiched between flexible Cu electrodes and encapsulated by PET films for structural integrity and electrical insulation (Fabrication details in Figure S1). The active dielectric is constructed via the face-to-face assembly of two single-layer patterned films, yielding a double-layer interlocked configuration with engineered interlayer air gaps. The PET films are used to improve the structural stability of the device and provide electrical insulation. Optical microscopy (Figure 1b(i)) confirms the successful replication of the staggered arrays and their seamless interlocking. Cross-sectional scanning electron microscopy (SEM) (Figure 1b(ii)) further reveals a well-distributed porous network across both the micro-protrusions and the bulk matrix, validating the efficacy of the glucose sacrificial templating method (geometric details in Figure S2). Macroscopically, this interlocked porous architecture exhibits excellent elastic compressibility and shape recovery (Figure 1c). To verify the synergistic effect of the hemispherical−conical staggered structure and internal pores during compression, finite element simulation was used to analyze the mechanical response behavior of HI-HCPS. As shown in Figure 1d, under external loading, the structural design of the sensor helps disperse local stress and improve the compressibility of the dielectric layer. To further validate this structural advantage, finite element simulations were conducted for four dielectric layer configurations (only hemisphere, only cone, dense non-porous structure, and hemisphere-cone porous structure) at pressures of 1 kPa, 30 kPa, and 200 kPa. The results shown in Figures S3 and S4 demonstrate that the hemisphere-cone porous structure exhibits higher initial sensitivity under low pressure while maintaining sustained deformation capability even at high pressures, whereas the single configurations are insufficient to achieve a balance between the two across the entire pressure range. These results indicate that the hemispherical−conical structure, double-layer interlocked interface, and internal pores can synergistically participate in load transfer and deformation buffering, providing a mechanical basis for subsequent pressure response tests. MWCNTs as conductive fillers with a high aspect ratio are incorporated into the PDMS matrix to construct filler networks within the composite dielectric layer and enhance interfacial polarization, thereby increasing the effective dielectric response of the material. According to the parallel-plate capacitance equation, $C = \varepsilon_0\varepsilon_r A/d$, when the effective overlapping area A of the upper and lower electrodes remains nearly unchanged, the capacitance variation of the dielectric layer mainly depends on changes in the electrode spacing d and the equivalent dielectric constant ε_r of the dielectric layer, where ε_0 is the vacuum permittivity.[29]

Figure 1e illustrates the response mechanism of the sensor under different pressure stages. In the low-pressure stage (Figure 1e(i)), the conical protrusions undergo preferential local compression due to tip-induced stress concentration, allowing a small pressure to induce an obvious thickness change. Meanwhile, the interlayer gaps and internal pores begin to shrink, leading to a rapid decrease in the electrode spacing d and thus a fast increase in capacitance. As the pressure further

Downloaded from pubs.acs.org/aamick/article-pdf/18/33/45605/6650371 1/am-2026-10724g.pdf by KOREA UNIV user on 23 September 2026

https://doi.org/10.1021/acsami.6c10724
ACS Appl. Mater. Interfaces 2026, 18, 45605−45617

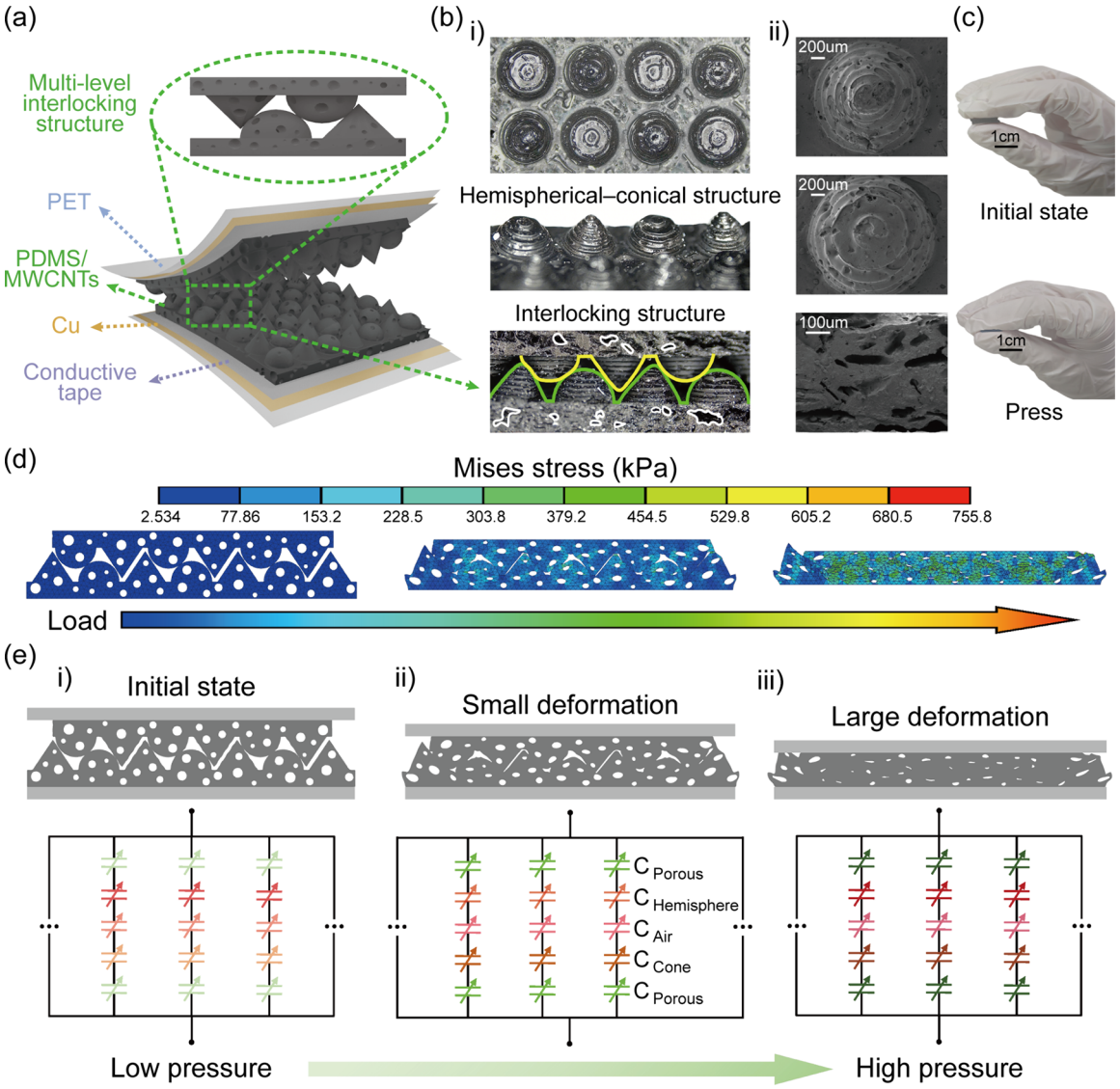


Figure 1. Structural design and sensing mechanism of HI-HCPS. (a) Structural schematic of HI-HCPS. (b) Morphological characterization of the sensor. (c) Elastic deformation and recovery of the double-layer interlocked dielectric layer. (d) Finite element simulation results of the stress distribution in the dielectric layer under external loading. (e) Pressure response mechanism of HI-HCPS during staged compression.

increases (Figure 1e(ii)), the local deformation of the conical protrusions gradually stabilizes, while the hemispherical protrusions begin to play a more dominant role in elastic support and sustained compression, promoting further closure of the double-layer interlocked interface. At the same time, the internal pores continue to shrink, reducing the proportion of the low-dielectric air phase and relatively increasing the effective fraction of the PDMS/MWCNT composite phase, thereby increasing the equivalent dielectric constant ε_r. Therefore, the capacitance variation in this stage mainly arises from the synergistic effect of reduced electrode spacing and enhanced equivalent dielectric constant. When the pressure further increases to a higher level (Figure 1e(iii)), the hemispherical−conical protrusions and internal pores gradually approach densification, and the available compressible space decreases. Nevertheless, the residual pores and the PDMS/MWCNT composite matrix still retain certain compressive deformability, enabling the sensor to maintain a continuous and stable capacitive response over a wide pressure range. The above-mentioned hierarchical compression and pore dielectric regulation mechanism provides the structural basis for achieving sensitive responses at low pressures and stable responses at high pressures, thereby enabling wide-range pressure detection.

2.2. Structural and Material Optimization

The sensing performance of the sensor was evaluated using a customized compression platform, an LCR digital bridge, and a computer (Figure S5). The sensitivity (S) of the capacitive sensor can be expressed as $S = (\Delta C/C_0)/\Delta P$, where C_0 is the initial capacitance under zero pressure, $\Delta C = C - C_0$ is the capacitance change under applied pressure, and P is the external pressure applied to the sensor.[30] To optimize the dielectric response and mechanical compressibility of the composite dielectric layer, the effect of different MWCNT contents on the sensing performance of HI-HCPS was compared. As shown in Figure 2a, when the MWCNT content increased from 1 to

https://doi.org/10.1021/acsami.6c10724
ACS Appl. Mater. Interfaces 2026, 18, 45605−45617

Downloaded from pubs.acs.org/aamick/article-pdf/18/33/45605/6650371 1/am-2026-10724g.pdf by KOREA UNIV user on 23 September 2026

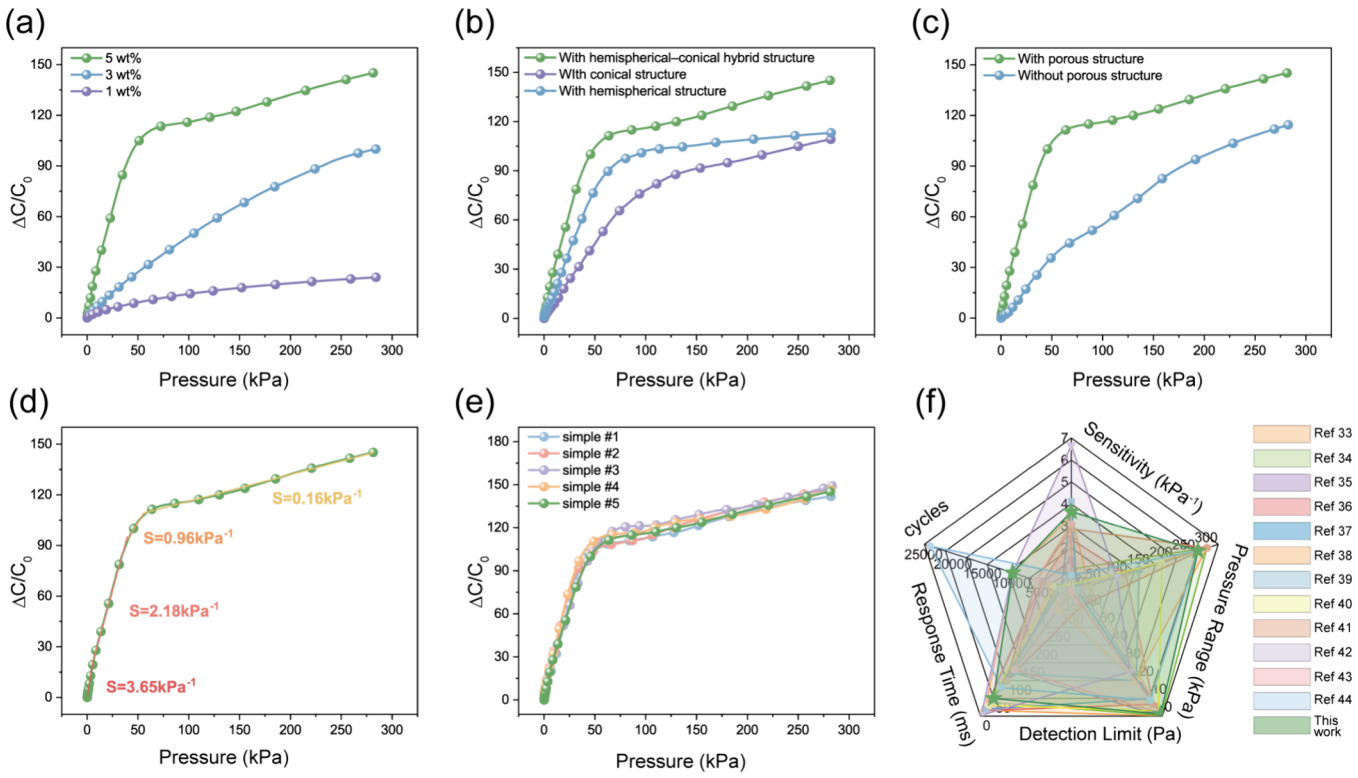


Figure 2. Structural and material optimization of HI-HCPS. (a) Sensitivity comparison of different MWCNT contents. (b) Sensitivity comparison of different structures. (c) Sensitivity comparison of dielectric layers with and without internal porous structures. (d) Capacitive response curve of HI-HCPS. (e) Relative capacitance changes of five different samples. (f) Comparison of HI-HCPS with previously reported sensors in terms of sensitivity, detection range, detection limit, response time, and cycling stability.

5 wt %, the normalized capacitive response of HI-HCPS gradually increased, indicating that the incorporation of MWCNTs can enhance the interfacial polarization effect and effective dielectric response of the composite dielectric layer. In contrast, the 7 wt % MWCNT sample showed response plateauing and signal fluctuation in the medium- and high-pressure regions (Figure S6), which may be related to filler aggregation caused by excessive loading, the composite system approaching a percolation state, and reduced compliance of the dielectric layer.[31,32] To further investigate the effect of MWCNT content on the mechanical properties of the composite dielectric layer, tensile tests were conducted on porous PDMS/MWCNT composite dielectric layers containing 1, 3, 5, and 7 wt % MWCNTs. The Young's modulus of each sample was subsequently calculated from the corresponding stress−strain curves, and the results are presented in Figure S7. Considering the above, the 5 wt % MWCNT sample exhibited a more continuous and stable wide-range capacitive response; therefore, it was selected as the optimized filler concentration for subsequent fabrication. To further verify the design advantages of the hemispherical−conical staggered structure, pure hemispherical protrusion and pure conical protrusion structures were fabricated as controls, and their capacitive responses were compared under the same testing conditions. Figure 2b shows the normalized capacitive response curves of the hemispherical, conical, and hemispherical−conical staggered structures. The microscope visually presents the hemispherical and conical protrusion structures (Figure S8). The results show that, under the same applied pressure, the relative capacitance change of the hemispherical−conical staggered structure is generally higher than that of the single-geometry structures, indicating superior response capability. The pure hemispherical structure exhibits good deformation reversibility and elastic support capability. However, its curved surface undergoes a relatively gradual compression process, resulting in limited thickness variation under low pressure and thus a relatively weak initial response. The pure conical structure is more prone to local compressive deformation in the low-pressure region due to the tip-induced stress concentration effect, which is beneficial for improving the initial response. However, as the pressure further increases, the conical tips gradually become compacted, and the available compressible space decreases, leading to a reduced response increment in the medium- and high-pressure regions. In contrast, the hemispherical−conical staggered structure combines the rapid low-pressure response of conical protrusions with the stable support effect of hemispherical protrusions in the medium- and high-pressure regions. This structure can form a graded compression mechanism at different pressure stages, allowing the dielectric layer to continuously generate effective capacitance changes over a broader pressure range. Therefore, through the functional complementarity of the two geometric units, the hemispherical−conical staggered structure improves the response continuity of HI-HCPS over a wide pressure range. To clarify the contribution of the internal porous structure to the pressure response, the capacitive responses of the solid dielectric layer and porous dielectric layer were first compared (Figure 2c). The results show that the porous dielectric layer produces higher relative capacitance changes than the solid dielectric layer over the entire pressure range. This can be attributed to two factors. On

Downloaded from pubs.acs.org/aamick/article-pdf/18/33/45605/6650371 1/am-2026-10724g.pdf by KOREA UNIV user on 23 September 2026

https://doi.org/10.1021/acsami.6c10724
ACS Appl. Mater. Interfaces 2026, 18, 45605−45617

the one hand, the internal pores reduce the effective stiffness of the composite dielectric layer, making it more susceptible to compressive deformation under external pressure and thereby inducing a more pronounced decrease in electrode spacing. On the other hand, the air inside the pores has a low dielectric constant. During compression, the pores gradually shrink, reducing the proportion of the low-dielectric air phase and relatively increasing the effective fraction of the PDMS/MWCNT composite phase, which increases the equivalent dielectric constant of the dielectric layer during compression.

After verifying the effectiveness of the porous structure, the effect of different glucose sacrificial template contents on the sensing performance of HI-HCPS was further compared (Figure S9). When the glucose content was 20 wt %, the number of pores was relatively low, resulting in limited compressible space and an insignificant improvement in capacitive response. When the content increased to 30 wt %, an appropriate amount of pores improved the compressibility of the dielectric layer and enhanced the capacitive response through pressure-induced pore shrinkage. In contrast, 40 wt % glucose introduced excessive pores, which weakened the continuity and mechanical support capability of the composite matrix, leading to a limited increase in response or even response plateauing. Therefore, 30 wt % glucose achieved a good balance between pore compressibility and structural stability and was selected as the sacrificial template content for subsequent fabrication. Based on the above material and structural optimization, HI-HCPS exhibits a continuous pressure response over the range of 0−280 kPa, with distinct segmented sensitivity characteristics (Figure 2d): 3.65 kPa^{-1} at 0−6 kPa, 2.18 kPa^{-1} at 6−30 kPa, 0.96 kPa^{-1} at 30−55 kPa, and 0.16 kPa^{-1} at 55−280 kPa. This wide-range response capability enables HI-HCPS to cover both weak low-pressure signal detection and medium- to high-pressure monitoring. To verify the repeatability of the sensor fabrication process, five independent samples were prepared under the same processing conditions, and their performances were compared (Figure 2e). The results show that the normalized capacitive response curves of the five samples remain generally consistent, indicating good batch-to-batch stability of the constructed hemispherical−conical staggered porous dielectric layer. The error-bar analysis in Figure S10 further shows that the response fluctuation at each pressure point is relatively small, and a stable variation trend is maintained even in the medium- and high-pressure regions, demonstrating the good reproducibility of this fabrication process. HI-HCPS was further compared with previously reported sensors (Figure 2f, Table S1).[33−44] The results show that HI-HCPS achieves a good balance among sensitivity, detection range, detection limit, response time, and cycling stability. These results provide a performance basis for subsequent wearable pressure monitoring and array-based pressure distribution recognition.

2.3. Sensing Performance

Based on the above material and structural optimization results, the hemispherical−conical staggered porous sensor prepared with 5 wt % MWCNTs and 30 wt % glucose sacrificial template was selected for subsequent performance tests. As shown in Figure 3a, the sensor can clearly detect a weak pressure stimulus generated by two 1 cm square paper pieces cut from 75 g m^{-2} A4 paper, with a total mass of approximately 0.015 g, corresponding to a pressure of about 1.22 Pa, and outputs a stable and distinguishable capacitive response. This result indicates that HI-HCPS can distinguish weak pressure stimuli at the pascal level. The dynamic response test of the sensor shows a response time of 50 ms and a recovery time of 100 ms (Figure 3b). To investigate the dynamic response stability of the sensor, Figure 3c presents the continuous loading−-unloading capacitive responses under different pressures of 1, 30, 80, and 150 kPa. During five cycles, the sensor produces stable and reversible capacitive responses to each pressure, with clear distinction among different pressure signals. The sensor exhibits a certain degree of hysteresis during the loading−unloading process, with a hysteresis rate of 10.94% (Figure 3d). This phenomenon may originate from viscoelastic dissipation in the PDMS/MWCNT composite dielectric layer, delayed rebound of the internal pores, and interfacial friction between the two interlocked dielectric layers.[45] During loading, the hemispherical−conical structure and internal pores undergo compressive deformation, reducing the thickness of the dielectric layer and increasing the capacitance. During unloading, the recovery of the PDMS matrix, air refilling in the pores, and interfacial friction between the double-layer interlocked interfaces all exhibit delayed behavior, making it difficult for the dielectric layer to instantaneously return to its initial state and thus resulting in a difference between the loading and unloading curves. To further investigate the influence of structural parameters on hysteresis behavior, comparative experiments were conducted under different porosity levels (non-porous, 20 wt %, and 30 wt % glucose-template structures) and different microstructural geometries (pure hemispherical, pure conical, and hemisphere−cone interlaced structures). The results shown in Figures S11 and S12 indicate that both porous architecture and microstructural geometry have a significant impact on the hysteresis characteristics, further validating the underlying mechanism from a structural design perspective. Referring to previously reported PDMS-based flexible capacitive pressure sensors, the hysteresis level of the present work falls within a typical range.[46−48] In dynamic sensing applications such as human motion monitoring, health monitoring, and electronic skin, such hysteresis is generally considered acceptable,[14] as these applications place greater emphasis on signal variation trends and repeatability rather than absolute point accuracy. Nevertheless, both the loading and unloading curves maintain continuous variation, indicating that the device can be used for stable pressure monitoring.

In addition, the sensor maintains distinguishable pressure responses under different preload conditions. Figure 3e shows the capacitive response characteristics of the sensor under preloads of 1, 30, and 50 kPa. Under a relatively low preload of 1 kPa, the device can distinguish a pressure increment of 0.1 kPa. Under higher preloads of 30 and 50 kPa, the device can still identify a pressure variation of 1 kPa (Figure S13). These results indicate that the sensor can not only respond to small pressure disturbances in the low-pressure region but also maintain a certain pressure resolution capability under higher preload conditions. To evaluate the frequency response characteristics of the sensor, cyclic loading tests at different frequencies were performed under a peak pressure of 50 kPa. As shown in Figure 3f, when the loading frequency increased from 0.05 to 0.8 Hz, the output signals of the sensor remained stable without obvious distortion or amplitude attenuation, indicating good dynamic pressure response capability. In addition, the sensor was subjected to 10,000 loading−unloading

Downloaded from pubs.acs.org/aamick/article-pdf/18/33/45605/6650371 1/am-2026-10724g.pdf by KOREA UNIV user on 23 September 2026

https://doi.org/10.1021/acsami.6c10724
ACS Appl. Mater. Interfaces 2026, 18, 45605−45617

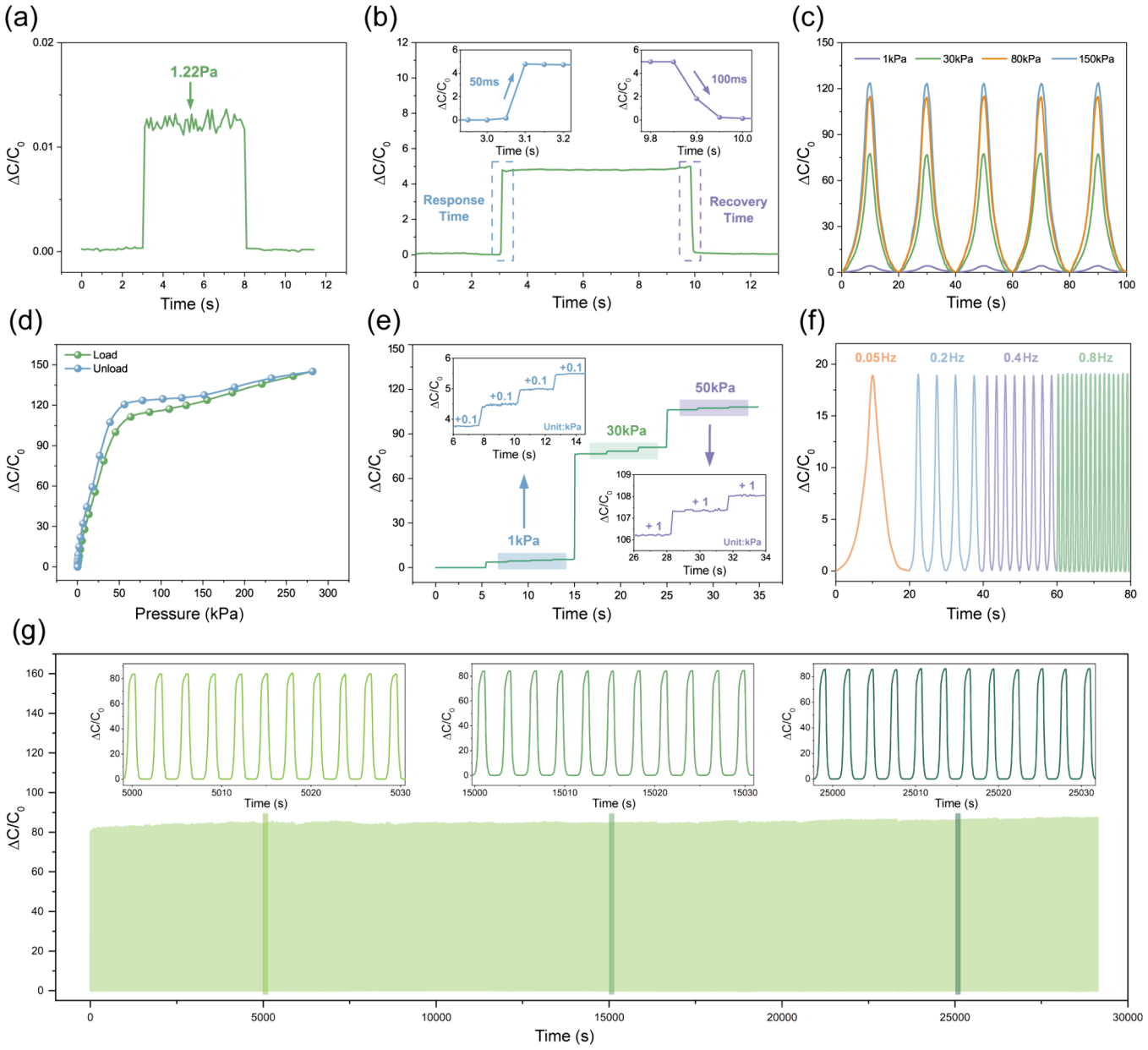


Figure 3. Sensing performance of HI-HCPS. (a) Response of HI-HCPS to weak pressure stimuli. (b) Dynamic response and recovery characteristics of HI-HCPS. (c) Capacitive response of HI-HCPS under different pressures. (d) Loading−unloading capacitive response of HI-HCPS (hysteresis rate = 10.94%). (e) Stepwise pressure response of HI-HCPS under different preload conditions. (f) Dynamic response of HI-HCPS to different loading frequencies (peak pressure = 50 kPa). (g) Durability test of HI-HCPS over 10,000 cycles under a load of 95 kPa.

cycles under a pressure of 95 kPa (Figure 3g). During the cycling test, no obvious drift or attenuation was observed in the capacitive response, demonstrating good long-term operational stability. To avoid lateral sliding of the double-layer interlocked structure during long-term cyclic loading, the sensor was tested with tight encapsulation (Figure S14). The initial preload introduced by encapsulation may slightly increase C_0, resulting in a certain difference in $\Delta C/C_0$ between the cycling test and the unencapsulated state. Furthermore, to evaluate the influence of environmental factors on sensor performance, the capacitance response of the sensor was systematically investigated under different temperatures (20, 30, 40, 50, and 60 °C) and relative humidity levels (40%, 50%, 60%, 70%, and 80% RH). As shown in Figures S15 and S16, only slight variations in the capacitance response were observed over the investigated temperature and humidity ranges, indicating that the fabricated sensor possesses excellent environmental stability. In addition, Figure S17 further shows the capacitive responses of the sensor under nonplanar deformation conditions, such as bending and twisting. The results indicate that HI-HCPS can still maintain distinguishable capacitance changes under external mechanical disturbances, demonstrating a certain degree of structural adaptability for pressure monitoring in flexible attachment and complex deformation scenarios. Moreover, the temperature-induced variation of C_0 can be effectively compensated through baseline

Downloaded from pubs.acs.org/aamick/article-pdf/18/33/45605/6650371 1/am-2026-10724g.pdf by KOREA UNIV user on 23 September 2026

https://doi.org/10.1021/acsami.6c10724
ACS Appl. Mater. Interfaces 2026, 18, 45605−45617

calibration at the operating temperature, ensuring sensor stability under actual operating conditions.

2.4. Wearable Physiological Signal and Human Motion Monitoring

Based on its low detection limit, wide pressure response range, and fast dynamic response capability, HI-HCPS can be used to detect human-related pressure signals with different amplitudes. To verify its applicability in wearable monitoring, the response capability of HI-HCPS to low-amplitude physiological signals was first investigated. As shown in Figure 4a, HI-HCPS can identify weak airflow disturbances generated by a rubber suction bulb, indicating its high response capability to low-load dynamic pressure. When HI-HCPS is fixed inside a face mask, it can capture periodic pressure fluctuations generated during respiration (Figure 4c). When attached to the abdominal skin, its output signals can reflect abdominal wall movement caused by abdominal respiration and remain consistent with the breathing rhythm (Figure 4f). Furthermore, when HI-HCPS is attached to the throat skin, it can identify local pressure changes caused by tongue-root lifting and swallowing, producing characteristic waveforms corresponding to these actions (Figure 4b,d). When HI-HCPS is worn over the radial artery at the wrist, it can capture pulse signals and distinguish typical pulse wave features, including the P, T, and D peaks (Figure 4e), indicating the potential of HI-HCPS for monitoring low-amplitude physiological processes.

In addition, HI-HCPS can also respond to larger-amplitude pressure changes generated by limb motion and hand grip-force interactions. When HI-HCPS is fixed on the finger, wrist, and elbow joints, the output signals of the sensor show distinguishable capacitive responses with changes in joint bending amplitude (Figure 4g–i), indicating its capability for dynamic monitoring of human motion states. In hand force-interaction scenarios, the capacitive response of HI-HCPS exhibits stepwise changes as the mass of the grasped load increases, enabling the distinction of different gripping-force levels (Figure 4j). The corresponding attachment methods, standard weights, and loading states are shown in Figure S18. Furthermore, when HI-HCPS is attached to the finger and used to press a polyurethane sponge and a medical absorbent cotton ball, its output signal increases with increasing pressing force (Figure 4k,l), indicating that HI-HCPS can be used to monitor pressure changes during the gripping of soft objects. These results indicate that HI-HCPS can output distinguishable capacitive responses to low-amplitude physiological signals, larger-amplitude human motions, and grip-force interactions, validating its applicability as a wearable pressure sensor.

2.5. Pressure Distribution Mapping of the HI-HCPS Array

To verify the array integration capability and pressure distribution sensing capability of the hemispherical–conical staggered porous sensor, a 3 × 5 flexible capacitive sensor array was constructed. Figure 5a shows the structural schematic of the sensor array, which consists of a silicone rubber substrate, Cu electrode layers, and hemispherical–conical staggered porous dielectric layers. The specific positioning and assembly method, the array wiring schematic of the circuit system, and the functional schematic of each module are shown in Figures S19–S21, respectively. To evaluate the crosstalk characteristics between array units, fixed-point pressing tests were performed at designated positions (Figure 5b). When target position 2 was pressed, the target unit produced an obvious capacitive response, whereas the adjacent units showed only weak signal changes. The calculated maximum crosstalk was approximately 5.37%, indicating low signal crosstalk between adjacent sensing units in the array and a negligible influence on pressure distribution detection. Furthermore, 3D-printed letter blocks (“L”, “U”, “C”, “K”, and “Y”) were applied to the surface of the sensor array as pressure sources to verify its pressure distribution mapping capability (Figure 5c and Figure S22). The corresponding pressure distribution heat maps clearly reconstructed the letter contours, with the main responses concentrated in the pressed regions and no obvious interference signals observed in the unpressed regions. These results indicate that the 3 × 5 sensor array can achieve low-crosstalk pressure distribution recognition, providing a basis for subsequent integration of the array onto a chair back for sitting posture pressure distribution monitoring.

2.6. Machine Learning-Assisted Sitting Posture Recognition

Long-term poor sitting posture can alter the pressure distribution on the back and may cause problems such as lumbar and back muscle fatigue.[49,50] Therefore, real-time monitoring of pressure distribution on the chair back is important for sitting posture assessment. Different sitting postures change the contact state between the human back and the chair back, resulting in distinct spatial pressure distributions. Based on the pressure mapping capability of the array, the 3 × 5 flexible sensor array was attached to the middle-lower region of the chair back to collect back-pressure responses under different sitting postures (Figure 6a), and the corresponding photograph is shown in Figure S23.

Five typical sitting postures were selected as recognition targets, including normal sitting, hunchback sitting, slouched sitting, left-leaning sitting, and right-leaning sitting. Figure 6b shows the pressure distribution heat maps under different sitting postures. Under normal sitting, the back-pressure distribution is relatively uniform (Figure 6b(i)). In the hunchback sitting posture, spinal curvature enhances the pressure response in the middle-lower region of the chair back (Figure 6b(ii)). In the reclined slouching sitting posture, backward leaning of the body shifts the pressure distribution toward the upper region of the chair back (Figure 6b(iv)). Left-leaning and right-leaning sitting postures produce more obvious pressure concentration regions on the left and right sides of the chair back, respectively (Figure 6b(iii),(v)). These differentiated responses indicate that the sensor array can convert different sitting postures into distinguishable spatial capacitance signals. The real-time pressure responses during posture transitions are shown in Video S1, further demonstrating that the array can capture dynamic sitting posture changes. To achieve effective recognition of sitting postures, a backpropagation (BP) neural network classification model was constructed based on the pressure distribution data collected by the chair back sensor array (Figure 6c). A total of 12 volunteers with different genders and body weights were recruited, and nearly 20,000 valid data samples were collected, covering five sitting states: normal sitting, hunchback sitting, slouched sitting, left-leaning sitting, and right-leaning sitting. Each sample consisted of signals from 15 sensing units in the 3 × 5 array. The dataset was randomly divided into training, validation, and test sets at a ratio of 80%, 10%, and 10%, respectively. During training, the

Downloaded from pubs.acs.org/aamick/article-pdf/18/33/45605/6650371 1/am-2026-10724g.pdf by KOREA UNIV user on 23 September 2026

https://doi.org/10.1021/acsami.6c10724
ACS Appl. Mater. Interfaces 2026, 18, 45605–45617

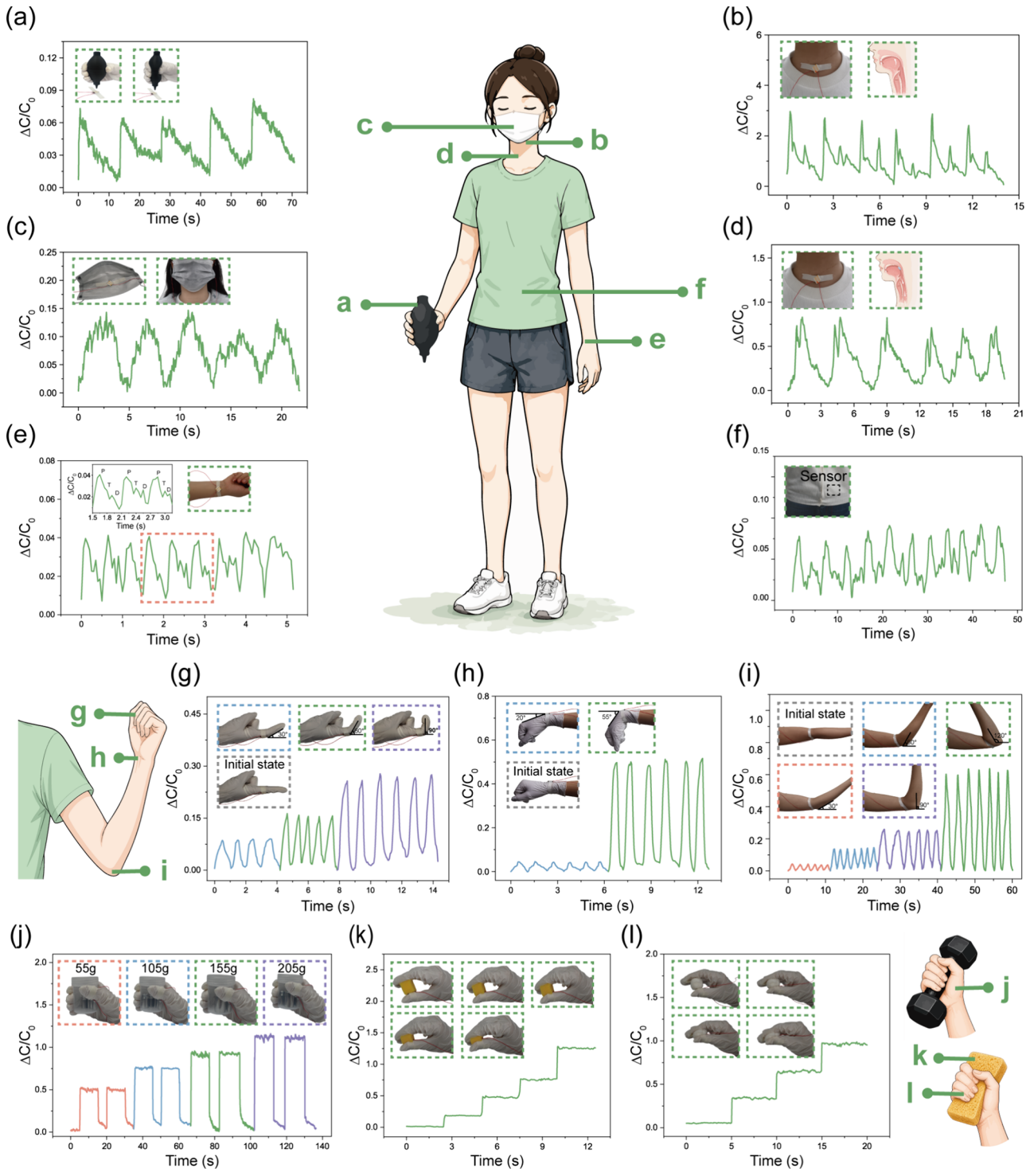


Figure 4. HI-HCPS for wearable physiological signal and human motion monitoring. (a) Response of HI-HCPS to weak airflow disturbances. (b) HI-HCPS attached to the throat region for tongue-root lifting monitoring. (c) HI-HCPS fixed inside a face mask for respiration monitoring. (d) HI-HCPS attached to the throat region for swallowing detection. (e) HI-HCPS for wrist pulse signal monitoring. (f) HI-HCPS attached to the abdomen for abdominal respiration monitoring. (g–i) HI-HCPS for monitoring finger, wrist, and elbow joint motions. (j) HI-HCPS for recognizing different gripping-force levels. (k, l) HI-HCPS for monitoring soft-object (polyurethane sponge and a medical absorbent cotton ball.) gripping processes.

cross-entropy loss decreased rapidly with increasing epochs and gradually converged (Figure 6d), indicating that the model could learn the pressure distribution features corresponding to different sitting postures. The confusion matrix of the test set showed that the overall classification accuracy for the five sitting postures reached 98.82% (Figure 6e). A small number of misclassifications may mainly arise from overlapping pressure distribution patterns between adjacent postures, such as normal sitting and slight leaning, or hunchback sitting and slouched sitting, which share certain similarities in local contact regions.

https://doi.org/10.1021/acsami.6c10724
ACS Appl. Mater. Interfaces 2026, 18, 45605–45617

Downloaded from pubs.acs.org/aamick/article-pdf/18/33/45605/6650371 1/am-2026-10724g.pdf by KOREA UNIV user on 23 September 2026

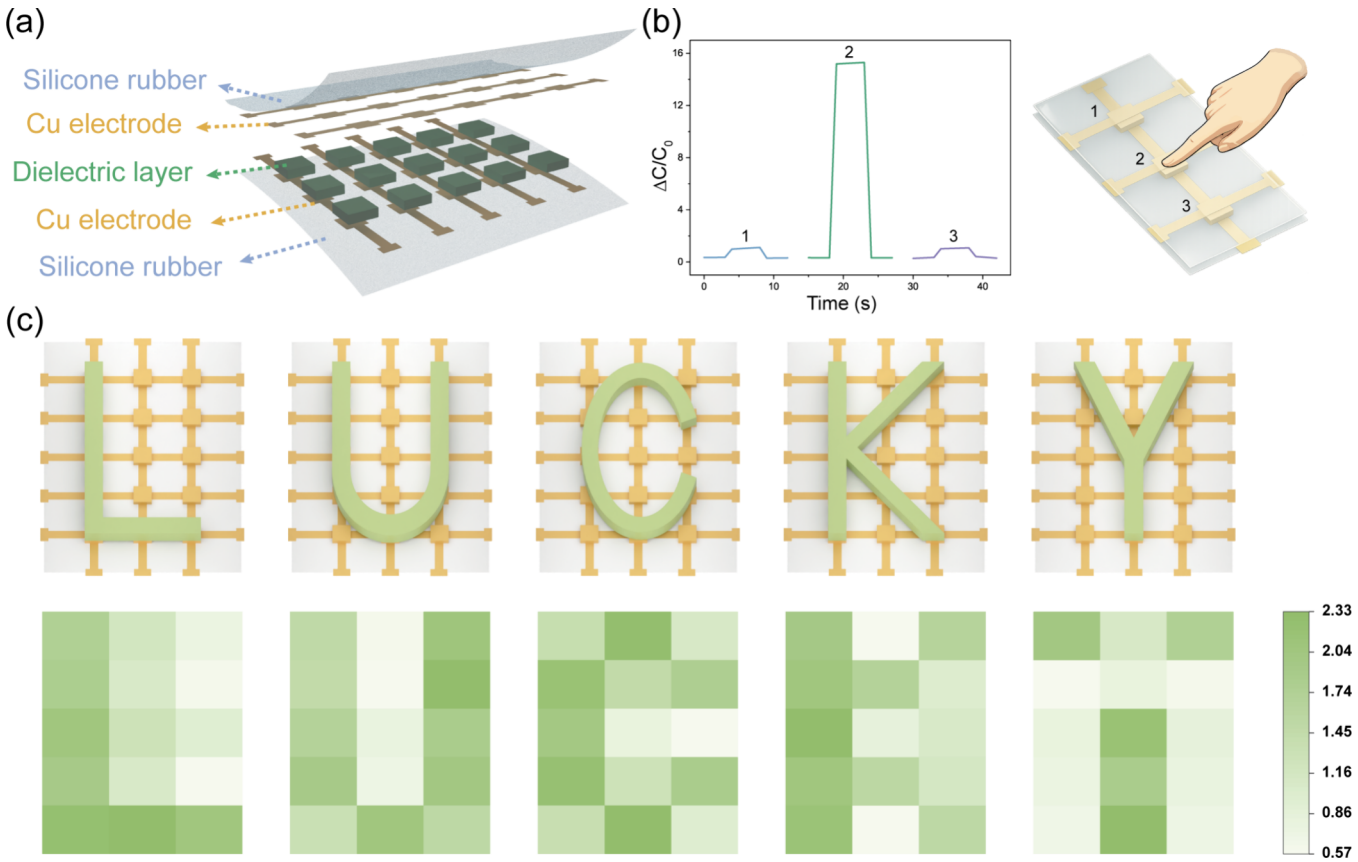


Figure 5. Pressure distribution mapping of a 3 × 5 HI-HCPS array. (a) Structural schematic of the 3 × 5 HI-HCPS array. (b) Crosstalk test between adjacent array units (crosstalk 5.37%). (c) Pressure mapping results of the sensor array under different 3D-printed letter blocks ("L", "U", "C", "K", and "Y").

These results demonstrate that the combination of the flexible sensor array and machine learning model can effectively recognize different sitting postures, providing a feasible method for pressure distribution monitoring in intelligent seating scenarios.

3. CONCLUSIONS

In summary, this work developed a flexible capacitive pressure sensor based on a double-layer interlocked hemispherical−conical staggered porous dielectric structure, namely, HI-HCPS. This structure synergistically integrates hemispherical protrusions, conical protrusions, and internal pores into a PDMS/MWCNT composite dielectric layer. Through multistage deformation mechanisms, including local contact enhancement, interlayer interlocked compression, and pore collapse, the sensor achieves an improved continuous capacitive response over a wide pressure range. As a result, HI-HCPS exhibits a low-pressure sensitivity of 3.65 kPa^{-1}, a detection range of 0−280 kPa, a detection limit of 1.22 Pa, response/recovery times of 50/100 ms, and stable output after 10,000 loading−unloading cycles, indicating a good overall balance among sensitivity, detection range, dynamic response, and stability. Further wearable and array-based application demonstrations show that HI-HCPS can meet multiscale pressure monitoring demands ranging from low-amplitude physiological signals to larger-amplitude human motions and grip-force interactions. Its 3 × 5 array enables low-crosstalk pressure distribution mapping and, combined with machine learning, recognizes five typical sitting postures with an overall classification accuracy of 98.82%. Overall, this work proposes a feasible bioinspired porous interlocked dielectric structure strategy, providing a new approach for constructing flexible capacitive pressure sensors with high sensitivity, wide-range response, and intelligent recognition capability, and showing application potential in wearable health monitoring, human−machine interaction, and intelligent sitting posture assessment.

4. EXPERIMENTAL SECTION

4.1. Materials

PDMS was purchased from Dow Corning Corporation. MWCNTs were sourced from Shenzhen Suiheng Technology Company, Ltd. Glucose was obtained from Kangmei Baoning Pharmaceutical Company, Ltd. Double-sided copper foil tape was acquired from Shenzhen Gongjin New Material Company, Ltd. Deionized water was purchased from Suzhou Weilit Environmental Protection Technology Co., Ltd. All reagents and materials were used as received without further purification.

4.2. Fabrication Process of the HI-HCPS Dielectric Layer

The dielectric layer is prepared through the following steps: First, the dielectric layer structure with hemispherical−conical protrusion arrays and the corresponding mold were designed using SolidWorks, and

Downloaded from pubs.acs.org/aamick/article-pdf/18/33/45605/6650371 1/am-2026-10724g.pdf by KOREA UNIV user on 23 September 2026

https://doi.org/10.1021/acsami.6c10724
ACS Appl. Mater. Interfaces 2026, 18, 45605−45617

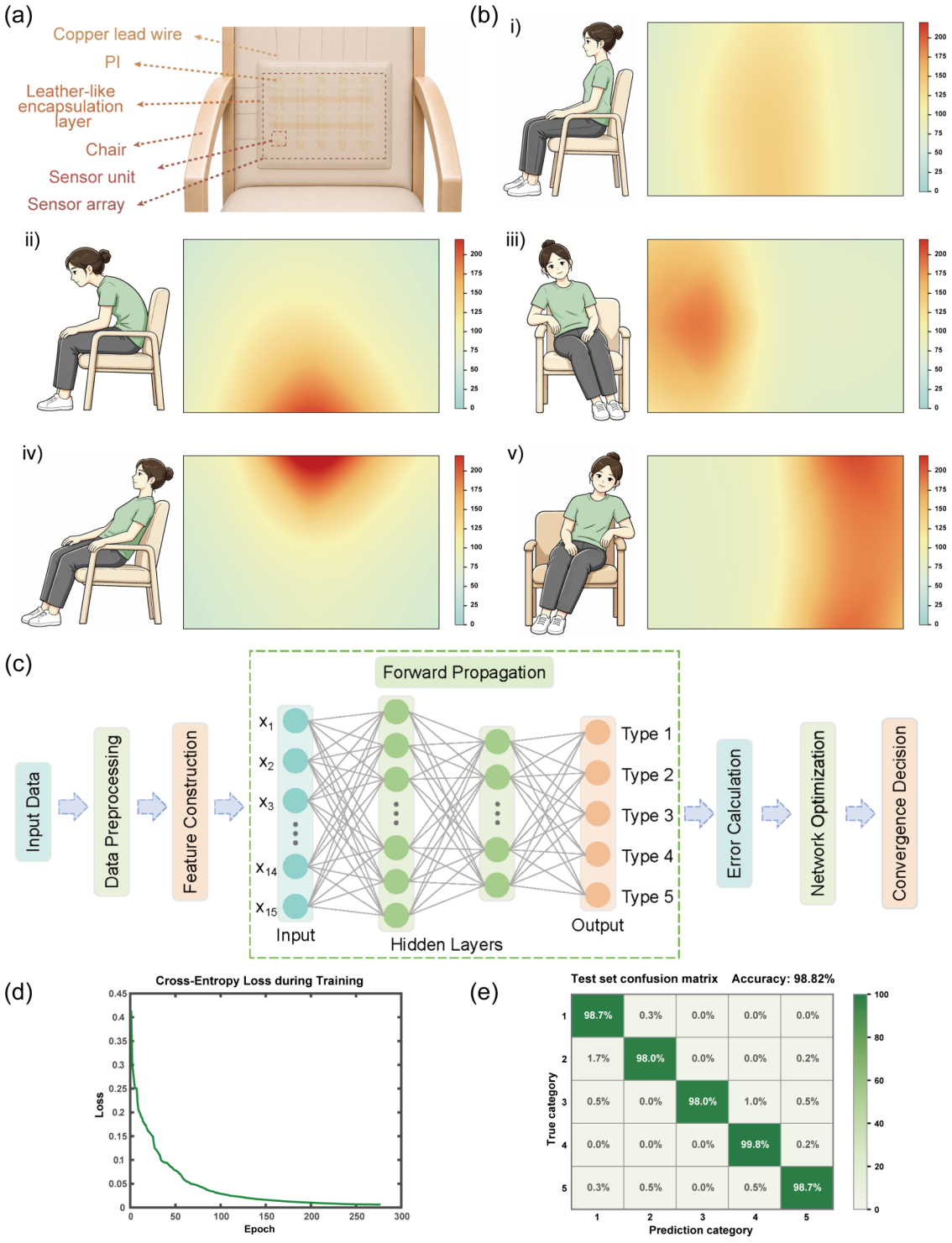


Figure 6. Sitting posture monitoring and machine learning-based recognition using the HI-HCPS array. (a) Schematic illustration of the HI-HCPS array attached to a chair back. (b) Pressure distribution maps corresponding to five typical sitting postures. (c) Flowchart of the backpropagation (BP) neural network. (d) Cross-entropy loss curve. (e) Test-set confusion matrix and recognition accuracy.

the resin forming mold was fabricated by a photocuring 3D printing process. The detailed structural parameters are provided in Figure S24. Subsequently, the PDMS base and curing agent were mixed at a mass ratio of 10:1, followed by the sequential addition of 5 wt % MWCNTs and 30 wt % glucose particles. The mixture was magnetically stirred at room temperature for 1 h and then ultrasonicated in an ice bath for 2 h to promote the uniform dispersion of the fillers and glucose particles in the PDMS matrix. The mixture was then transferred to a vacuum defoaming mixer and treated under vacuum at 1500 rpm for 120 s to obtain the PDMS/MWCNT/glucose composite prepolymer. The obtained composite prepolymer was filled into the cavity of the resin mold and cured in a drying oven at 80 °C for 6 h. After curing, the sample was demolded to obtain a composite dielectric layer precursor containing glucose particles. To remove the glucose,

https://doi.org/10.1021/acsami.6c10724
ACS Appl. Mater. Interfaces 2026, 18, 45605−45617

Downloaded from pubs.acs.org/aamick/article-pdf/18/33/45605/6650371 1/am-2026-10724g.pdf by KOREA UNIV user on 23 September 2026

the precursor was completely immersed in deionized water at 90 °C, followed by magnetic stirring for 1 h and ultrasonication for 1 h to preliminarily dissolve the glucose particles on the surface and near-surface regions. Subsequently, the sample was kept under vacuum at 90 °C for 30 min to promote the infiltration of deionized water into the internal pores. After returning to atmospheric pressure, the sample was continuously magnetically stirred in deionized water at 90 °C for 8 h to sufficiently remove the internal glucose. Finally, the sample was ultrasonically cleaned in fresh deionized water for 1 h and dried at 80 °C for 2 h, yielding a PDMS/MWCNT composite dielectric layer with both surface hemispherical−conical staggered protrusions and internal porous structures.

4.3. Fabrication of HI-HCPS

The two prepared single-layer hemispherical−conical staggered porous dielectric layers were assembled face-to-face to form a double-layer heterogeneous interlocked composite dielectric layer. Subsequently, two Cu foil electrodes with dimensions of 1.3 cm × 1.3 cm were cut, and wires were connected to the edges of the Cu foils for capacitance signal acquisition. During assembly, the double-layer interlocked dielectric layer was sandwiched between the upper and lower Cu foil electrodes, ensuring alignment between the electrodes and the dielectric layer. Finally, the device was externally encapsulated with PET films for electrical insulation and structural protection, yielding a flexible capacitive pressure sensor.

4.4. Sensing Performance Tests

The capacitive response of the sensor was measured using an electromechanical compression testing platform combined with an LCR digital bridge. Mechanical pressure was applied by an electric compression testing platform (ESM303, Mark-10), and real-time capacitance signals were collected using an LCR digital bridge (TH2829C, Tonghui Electronics) and a data acquisition system. To minimize interference from low-frequency band interface polarization and contact impedance on capacitance measurements and to reduce measurement delays caused by frequency switching, this study uniformly adopts the widely used 100 kHz as the test frequency.

4.5. Dataset Collection for Machine Learning

A total of 12 volunteers, including 6 males and 6 females aged 18–45 years, were recruited for the sitting posture recognition experiment. During the experiment, the 3 × 5 flexible sensor array was fixed to the middle-lower region of the chair back to collect back-pressure distribution signals. Each volunteer sequentially performed five typical sitting postures, including normal sitting, hunchback sitting, slouched sitting, left-leaning sitting, and right-leaning sitting. Each posture was maintained for 3 min, while the capacitive responses of the 15 sensing units were recorded simultaneously. After preprocessing, the collected array signals were used to construct a sitting posture pressure dataset. Each sample consisted of the relative capacitive responses from the 15 sensing units in the 3 × 5 array, representing the spatial pressure distribution at the corresponding time point. After screening, nearly 20,000 valid samples were obtained. The dataset was randomly divided into training, validation, and test sets at a ratio of 80%, 10%, and 10%, respectively. A backpropagation (BP) neural network was used to classify the five sitting postures, and the model performance was evaluated using classification accuracy and a confusion matrix.

■ ASSOCIATED CONTENT

Supporting Information

The Supporting Information is available free of charge at https://pubs.acs.org/doi/10.1021/acsami.6c10724.

Fabrication process of the porous dielectric layer (Figure S1); three-dimensional modeled structure and dimensional annotations of the single-layer hemispherical−conical staggered dielectric layer (Figure S2); von Mises stress distributions of four dielectric layer structures under different applied pressures (Figure S3); equivalent strain distributions of four dielectric layer structures under different applied pressures (Figure S4); schematic of the capacitance−pressure testing platform (Figure S5); comparison of the relative capacitive response curves of HI-HCPS based on 5 wt % and 7 wt % MWCNTs (Figure S6); measurement diagrams of Young's modulus of porous PDMS/MWCNT composite dielectric layer at different concentrations (Figure S7); optical microscopy images of dielectric layers with different surface structures (Figure S8); relative capacitive response curves of HI-HCPS prepared with different glucose contents (Figure S9); error-bar analysis of the capacitive responses of five independent HI-HCPS samples (Figure S10); comparison of the sensing performance of HI-HCPS with reported flexible capacitive pressure sensors (Table S1); hysteresis performance test of dielectric layers with different glucose sacrificial template contents (Figure S11); hysteresis performance test of dielectric layers with different microstructure geometries (Figure S12); resolution under a preload of 30 kPa (Figure S13); schematic illustration of the encapsulation of a single sensor during cyclic loading tests (Figure S14); the influence of temperature on the performance of sensors (Figure S15); the influence of humidity on the performance of sensors (Figure S16); relative capacitive responses of the sensor under nonplanar mechanical deformation conditions (Figure S17); application demonstration of the sensor attached to the thumb for grip-force monitoring (Figure S18); positioning and assembly process of the 3 × 5 flexible capacitive sensor array (Figure S19); circuit schematic of the wiring configuration of the 3 × 5 flexible capacitive sensor array (Figure S20); photograph of the circuit board prototype with labeled functional modules (Figure S21); physical demonstration of letter-pattern loading on the 3 × 5 sensor array (Figure S22); photograph of the 3 × 5 sensor array installed on the chair back (Figure S23); geometrical dimensions of the 3D-printed mold microstructures (Figure S24) (DOCX)

Real-time capacitance response maps under different sitting postures (Video S1) (MP4)

■ AUTHOR INFORMATION

Corresponding Author

Zhi-Jun Zhao – *Institute of Smart City and Intelligent Transportation, Southwest Jiaotong University, Chengdu 611756, China*; orcid.org/0000-0002-4981-5062; Email: zhaozhijun@swjtu.edu.cn

Authors

Shiqi Wu – *Institute of Smart City and Intelligent Transportation, Southwest Jiaotong University, Chengdu 611756, China*

Yanyan Chen – *Institute of Smart City and Intelligent Transportation, Southwest Jiaotong University, Chengdu 611756, China*

Downloaded from pubs.acs.org/aamick/article-pdf/18/33/45605/6650371 1/am-2026-10724g.pdf by KOREA UNIV user on 23 September 2026

Jiawei Wu – *Southwest Jiaotong University-Leeds Joint School, Chengdu 611756, China*
Junseong Ahn – *Department of Control and Instrumentation Engineering, Korea University, Sejong 30019, Republic of Korea*; orcid.org/0000-0002-4090-5440
Yun-Woo Lee – *Department of Mechanical Engineering, Soongsil University 369 Sangdo-ro, Dongjak-Gu, Seoul 06978, Korea*
Hongbo Wang – *Institute of Smart City and Intelligent Transportation, Southwest Jiaotong University, Chengdu 611756, China*; orcid.org/0000-0002-8031-5533
Bingjun Yu – *Tribology Research Institute, School of Mechanical Engineering, Southwest Jiaotong University, Chengdu 610031, China*; orcid.org/0000-0002-8281-1899
Caijiang Lu – *Tribology Research Institute, School of Mechanical Engineering, Southwest Jiaotong University, Chengdu 610031, China*

Complete contact information is available at: https://pubs.acs.org/doi/10.1021/acsami.6c10724

Author Contributions

‡S.Q.W. and Y.Y.C. contributed equally to this work. They jointly conceived the research hypotheses, designed the experimental framework, performed finite element analysis, established the electrical testing setup, conducted the experiments, integrated and interpreted the data, developed the machine learning architectures, and drafted the initial manuscript. J.W.W. established the real-time heatmap imaging system. Z.-J.Z. provided critical academic guidance and oversaw the project's overall direction.

Notes

The authors declare no competing financial interest.

■ ACKNOWLEDGMENTS

This work was supported by the National Natural Science Foundation of China (no. 52375578) and Fundamental Research Funds for the Central Universities (2682025CG001)

■ ABBREVIATION

HI-HCPS	heterogeneous interlocked hemispherical-conical staggered porous sensor
PDMS	polydimethylsiloxane
MWCNTs	multiwalled carbon nanotubes
PET	polyethylene terephthalate
Cu	copper
SEM	scanning electron microscopy
BP	backpropagation
LCR	inductance−capacitance−resistance
3D	three-dimensional

■ REFERENCES

(1) Gao, W.; Ota, H.; Kiriya, D.; Takei, K.; Javey, A. Flexible Electronics toward Wearable Sensing. *Acc. Chem. Res.* **2019**, *52*, 523−533.
(2) Chen, S.; Qi, J.; Fan, S.; Qiao, Z.; Yeo, J. C.; Lim, C. T. Flexible Wearable Sensors for Cardiovascular Health Monitoring. *Adv. Healthcare Mater.* **2021**, *10*, e2100116.
(3) Jeon, S.; Lim, S. C.; Trung, T. Q.; Jung, M.; Lee, N. E. Flexible Multimodal Sensors for Electronic Skin: Principle, Materials, Device, Array Architecture, and Data Acquisition Method. *Proc. IEEE* **2019**, *107*, 2065−2083.
(4) Xu, C.; Chen, J.; Zhu, Z.; Liu, M.; Lan, R.; Chen, X.; Tang, W.; Zhang, Y.; Li, H. Flexible Pressure Sensors in Human-Machine Interface Applications. *Small* **2024**, *20*, e2306655.
(5) Wang, Y.; Wang, T.; Wu, Q.; Huang, Y. A Quasi-homogeneous-Integrated Flexible Proximity-Pressure Dual-Mode Sensor for Human Machine Interaction. *ACS Appl. Mater. Interfaces* **2026**, *18*, 11877−11889.
(6) Chen, B.; Zhang, L.; Li, H.; Lai, X.; Zeng, X. Skin-inspired flexible and high-performance MXene@polydimethylsiloxane piezoresistive pressure sensor for human motion detection. *J. Colloid Interface Sci.* **2022**, *617*, 478−488.
(7) He, W.; Zhang, Y.; Zhang, P.; Zheng, J.; Xue, B.; Hu, G.; Li, Z.; Wu, Y.; Zhang, R. Deep learning-assisted flexible piezoresistive sensor with liquid-phase reduced metal electrodes for fitness movement recognition and correction. *Chem. Eng. J.* **2024**, *495*, 153362.
(8) Yang, M.; Wang, Y.; Li, M.; Wang, B.; Sun, S.; Wan, C.; Ju, X. Self-powered flexible piezo-photoelectric dual-mode sensor based on PVDF-TrFE combined with MXene@TiO2 heterojunction. *Composites, Part B* **2026**, *310*, 113161.
(9) Xu, Q.; Jia, M.; Zhou, P.; Zhang, Y.; Guo, W.; Zhao, S.; Zeng, H.; Zhang, J.; Yan, M.; Jiang, S.; Zhou, K.; Zhang, D.; Bowen, C. High-Performance Ultrasensitive Flexible Piezoelectric Thin Film Sensors via a Cost-Effective Transfer Strategy. *Adv. Funct. Mater.* **2025**, *35*, 2414211.
(10) Chiu, Y. S.; Rinawati, M.; Chang, Y. H.; Aulia, S.; Chang, C. C.; Chang, L. Y.; Hung, W. S.; Mizuguchi, H.; Haw, S. C.; Yeh, M. H. Enhancing self-induced polarization of PVDF-based triboelectric film by P-doped g-C3N4 for ultrasensitive triboelectric pressure sensors. *Nano Energy* **2024**, *131*, 110207.
(11) Zhou, H.; Gui, Y.; Gu, G.; Ren, H.; Zhang, W.; Du, Z.; Cheng, G. A Plantar Pressure Detection and Gait Analysis System Based on Flexible Triboelectric Pressure Sensor Array and Deep Learning. *Small* **2025**, *21*, e2405064.
(12) Liu, L.; Huang, X.; Zhao, K.; Jiang, G.; Cong, H.; Ramakrishna, S.; He, H. Interfacial polarization-enabled high anti-interference for fiber-based capacitive pressure sensors. *Chem. Eng. J.* **2025**, *518*, 164746.
(13) Basarir, F.; Haj, Y. A.; Zou, F.; De, S.; Nguyen, A.; Frey, A.; Haider, I.; Sariola, V.; Vapaavuori, J. Edible and Biodegradable Wearable Capacitive Pressure Sensors: A Paradigm Shift toward Sustainable Electronics with Bio-Based Materials. *Adv. Funct. Mater.* **2024**, *34*, 2403268.
(14) Wang, H.; Li, Z.; Liu, Z.; Fu, J.; Shan, T.; Yang, X.; Lei, Q.; Yang, Y.; Li, D. Flexible capacitive pressure sensors for wearable electronics. *J. Mater. Chem. C* **2022**, *10*, 1594−1605.
(15) Guo, Y.; Gao, S.; Yue, W.; Zhang, C.; Li, Y. Anodized Aluminum Oxide-Assisted Low-Cost Flexible Capacitive Pressure Sensors Based on Double-Sided Nanopillars by a Facile Fabrication Method. *ACS Appl. Mater. Interfaces* **2019**, *11*, 48594−48603.
(16) Ha, K. H.; Huh, H.; Li, Z.; Lu, N. Soft Capacitive Pressure Sensors: Trends, Challenges, and Perspectives. *ACS Nano* **2022**, *16*, 3442−3448.
(17) Zhong, Y.; Liu, K.; Wu, L.; Ji, W.; Cheng, G.; Ding, J. Flexible Tactile Sensors with Gradient Conformal Dome Structures. *ACS Appl. Mater. Interfaces* **2024**, *16*, 52966−52976.
(18) Zhao, K.; Han, J.; Ma, Y.; Tong, Z.; Suhr, J.; Wang, M.; Xiao, L.; Jia, S.; Chen, X. Highly Sensitive and Flexible Capacitive Pressure Sensors Based on Vertical Graphene and Micro-Pyramidal Dielectric Layer. *Nanomaterials* **2023**, *13*, 701.
(19) Han, K.; Kim, I.; Lee, E.; Bae, G. Y.; Yang, C. Liquid Metal Composite-Based Flexible Pressure Sensors with High Sensitivity. *ACS Appl. Mater. Interfaces* **2025**, *17*, 40994−41001.
(20) Xiong, Y.; Shen, Y.; Tian, L.; Hu, Y.; Zhu, P.; Sun, R.; Wong, C. P. A flexible, ultra-highly sensitive and stable capacitive pressure sensor with convex microarrays for motion and health monitoring. *Nano Energy* **2020**, *70*, 104436.

Downloaded from pubs.acs.org/aamick/article-pdf/18/33/45605/6650371 1/am-2026-10724g.pdf by KOREA UNIV user on 23 September 2026

(21) Thouti, E.; Nagaraju, A.; Chandran, A.; Prakash, P. V. B. S. S.; Shivanarayanamurthy, P.; Lal, B.; Kumar, P.; Kothari, P.; Panwar, D. Tunable flexible capacitive pressure sensors using arrangement of polydimethylsiloxane micro-pyramids for bio-signal monitoring. *Sens. Actuators, A* **2020**, *314*, 112251.
(22) Hua, T.; Xiang, Z.; Xia, X.; Li, Z.; Sun, D.; Wu, Y.; Liu, Y.; Shang, J.; Chen, J.; Li, R. A Sensitivity-Optimized Flexible Capacitive Pressure Sensor with Cylindrical Ladder Microstructural Dielectric Layers. *Sensors* **2023**; *23*, 4323.
(23) Jung, Y.; Lee, W.; Jung, K.; Park, B.; Park, J.; Ko, J.; Cho, H. A Highly Sensitive and Flexible Capacitive Pressure Sensor Based on a Porous Three-Dimensional PDMS/Microsphere Composite. *Polymers* **2020**, *12*, 1412.
(24) Hwang, J.; Kim, Y.; Yang, H.; Oh, J. H. Fabrication of hierarchically porous structured PDMS composites and their application as a flexible capacitive pressure sensor. *Composites Part B* **2021**, *211*, 108607.
(25) Kim, Y.; Yang, H.; Oh, J. H. Simple fabrication of highly sensitive capacitive pressure sensors using a porous dielectric layer with cone-shaped patterns. *Mater. Des.* **2021**, *197*, 109203.
(26) Laysandra, L.; Bazliah, D.; Sentosa, D. M.; Heksa, A. C.; Bui, H. K.; Li, Y. C.; Chiu, Y. C. The rise of rubber-like synthetic polymers in next-gen transistor technologies. *Chem. Sci.* **2025**, *16*, 20181−20228.
(27) Zeng, P.; Pan, P.; He, J.; Yang, Z.; Song, H.; Zhang, J. Porous Composite PDMS for a Pressure Sensor with a Wide Linear Range. *ACS Appl. Nano Mater.* **2024**, *7*, 455−465.
(28) Choi, J.; Kwon, D.; Kim, K.; Park, J.; Orbe, D. D.; Gu, J.; Ahn, J.; Cho, I.; Jeong, Y.; Oh, Y.; Park, I. Synergetic Effect of Porous Elastomer and Percolation of Carbon Nanotube Filler toward High Performance Capacitive Pressure Sensors. *ACS Appl. Mater. Interfaces* **2020**, *12*, 1698−1706.
(29) Yuan, H.; Zhang, Q.; Zhou, T.; Wu, W.; Li, H.; Yin, Z.; Ma, J.; Jiao, T. Progress and challenges in flexible capacitive pressure sensors: Microstructure designs and applications. *Chem. Eng. J.* **2024**, *485*, 149926.
(30) Bai, N.; Wang, L.; Wang, Q.; Deng, J.; Wang, Y.; Lu, P.; Huang, J.; Li, G.; Zhang, Y.; Yang, J.; Xie, K.; Zhao, X.; Guo, C. F. Graded intrafillable architecture-based iontronic pressure sensor with ultra-broad-range high sensitivity. *Nat. Commun.* **2020**, *11*, 209.
(31) Tang, Z. H.; Wang, D. Y.; Li, Y. Q.; Huang, P.; Fu, S. Y. Modeling the synergistic electrical percolation effect of carbon nanotube/graphene/polymer composites. *Compos. Sci. Technol.* **2022**, *225*, 109496.
(32) Zarei Darani, S.; Naghdabadi, R. An experimental study on multi-walled carbon nanotube nanocomposite piezoresistivity considering the filler agglomeration effects. *Polym. Compos.* **2021**, *42*, 4707−4716.
(33) Xiong, W.; Zhang, F.; Qu, S.; Yin, L.; Li, K.; Huang, Y. Marangoni-driven deterministic formation of softer, hollow microstructures for sensitivity-enhanced tactile system. *Nat. Commun.* **2024**, *15*, 5596.
(34) Guo, X.; Jin, C.; Li, X.; Zhang, A.; Hong, W.; Yan, Z.; Zhang, X.; Yu, S.; Yu, S.; Zhang, H.; Zhu, X.; Zong, H.; Du, Y.; Lu, H.; Zhao, Y.; Xu, Y. Electromechanical performance of flexible sensor based on 3D printed biomimetic all-PDMS-coated multistage structure: Toward kinesiology monitoring and human-machine interaction. *Sens. Actuators, A* **2024**, *369*, 115193.
(35) Lv, C.; Tian, C.; Jiang, J.; Dang, Y.; Liu, Y.; Duan, X.; Li, Q.; Chen, X.; Xie, M. Ultrasensitive Linear Capacitive Pressure Sensor with Wrinkled Microstructures for Tactile Perception. *Adv. Sci.* **2023**, *10*, No. e2206807.
(36) Zhao, Y.; Zhou, J.; Jiang, C.; Xu, T.; Li, K.; Zhang, D.; Sheng, B. Highly Sensitive and Flexible Capacitive Pressure Sensors Combined with Porous Structure and Hole Array Using Sacrificial Templates and Laser Ablation. *Polymers* **2024**, *16*, 2369.
(37) Lin, Y.; Yu, Z.; Xue, H.; Zhang, T.; Pan, T.; Gu, J.; Huang, F. Flexible capacitive pressure sensors with high sensitivity and durability via an electrohydrodynamic printing method. *J. Mater. Chem. C* **2026**, *14*, 3684−3695.
(38) Bin Lee, H.; Kim, S. W.; Jeong, H. Y.; Yang, Y. J.; Park, S. H.; Kang, C. U.; Kim, H. B. A flexible capacitive pressure sensor with a monolithically 3D-Printed arch-structured dielectric layer. *Addit. Manuf.* **2026**, *117*, 105080.
(39) Li, S.; Wang, Y.; Wu, Y.; Asghar, W.; Xia, X.; Liu, C.; Bai, X.; Shang, J.; Liu, Y.; Li, R. W. Piezo-Capacitive Flexible Pressure Sensor with Magnetically Self-Assembled Microneedle Array. *ACS Sens.* **2025**, *10*, 1063−1071.
(40) Jin, Z.; Dong, S.; Liu, X.; Zheng, X.; Guo, J.; Sung, H. K.; Chernogor, L.; Yao, Z.; Li, Y.; Li, Y. Hierarchical microstructure-enhanced flexible capacitive pressure sensor for high-accuracy fruit identification. *Chem. Eng. J.* **2025**, *520*, 166137.
(41) Xiao, Y.; Wu, X.; Yang, L.; Zhu, J. Fabrication of high-performance fabric-based capacitive pressure sensors with two-scale synergistic resistive/capacitive hybrid response. *J. Mater. Sci. Technol.* **2026**, *240*, 87−97.
(42) Ding, Y.; Shao, Y.; Xu, H.; Xiong, Z.; Luo, J.; Mao, Y.; Yang, P. a.; Huang, Z. A flexible capacitive sensor featuring spherical-like microstructures with ultrafast response and an ultralow detection limit for miniature fast steering mirror applications. *Chem. Eng. J.* **2026**, *534*, 174815.
(43) Fu, H.; Zhao, Z.; Jiang, J.; Chen, Y.; Zhang, H.; Li, H.; Liang, G. Tunable flexible capacitive sensor for dynamic pressure monitoring. *Microsyst. Nanoeng.* **2026**, *12*, 110.
(44) Hong, W.; Guo, X.; Zhang, T.; Zhang, A.; Yan, Z.; Zhang, X.; Li, X.; Guan, Y.; Liao, D.; Lu, H.; Liu, H.; Hu, J.; Niu, Y.; Hong, Q.; Zhao, Y. Flexible Capacitive Pressure Sensor with High Sensitivity and Wide Range Based on a Cheetah Leg Structure via 3D Printing. *ACS Appl. Mater. Interfaces* **2023**, *15*, 46347−46356.
(45) He, J.; Huang, J.; Li, R.; Chen, Z.; Li, Z.; Zhou, R.; Wang, S.; Gao, W.; Guo, C. F.; Bao, R.; Pan, C. Hysteresis-free and dynamically resilient strain sensor enabled by interfacial coordination. *Sci. Adv.* **2026**, *12*, eaea2450.
(46) Liu, S. Y.; Lu, J. G.; Shieh, H. P. D. Influence of Permittivity on the Sensitivity of Porous Elastomer-Based Capacitive Pressure Sensors. *IEEE Sens. J.* **2018**, *18*, 1870−1876.
(47) Shi, H.; Ren, K.; Jiang, H.; Wang, H.; Yu, B.; Qian, L.; Zhao, Z. J. Honeycomb-Shaped Flexible Capacitive Pressure Sensor with Ultrahigh Sensitivity and an Exceptionally Broad Linear Response Range. *ACS Appl. Mater. Interfaces* **2025**, *17*, 48563−48573.
(48) Ouyang, Y.; Lei, J.; Li, S.; He, G.; He, S. Highly Sensitive Capacitive Pressure Sensor Based on MWCNTs/TiO2/PDMS with a Microhemispherical Array and APTES-Modified Interface. *Polymers* **2025**, *18*, 12.
(49) Kett, A. R.; Sichting, F.; Milani, T. L. The Effect of Sitting Posture and Postural Activity on Low Back Muscle Stiffness. *Biomechanics* **2021**, *1*, 214−224.
(50) Cho, M.; Han, J. S.; Kang, S.; Ahn, C. H.; Kim, D. H.; Kim, C. H.; Kim, K. T.; Kim, A. R.; Hwang, J. M. Biomechanical Effects of Different Sitting Postures and Physiologic Movements on the Lumbar Spine: A Finite Element Study. *Bioengineering* **2023**, *10*, 1051.

Downloaded from pubs.acs.org/aamick/article-pdf/18/33/45605/6650371 1/am-2026-10724g.pdf by KOREA UNIV user on 23 September 2026

https://doi.org/10.1021/acsami.6c10724
ACS Appl. Mater. Interfaces 2026, 18, 45605−45617